

Technical University of Denmark



Smearred crack modelling approach for corrosion-induced concrete damage

Thybo, Anna Emilie Anusha; Michel, Alexander; Stang, Henrik

Published in:
Materials and Structures

Link to article, DOI:
[10.1617/s11527-017-0999-5](https://doi.org/10.1617/s11527-017-0999-5)

Publication date:
2017

Document Version
Peer reviewed version

[Link back to DTU Orbit](#)

Citation (APA):
Thybo, A. E. A., Michel, A., & Stang, H. (2017). Smearred crack modelling approach for corrosion-induced concrete damage. *Materials and Structures*, 50(146). DOI: 10.1617/s11527-017-0999-5

DTU Library
Technical Information Center of Denmark

General rights

Copyright and moral rights for the publications made accessible in the public portal are retained by the authors and/or other copyright owners and it is a condition of accessing publications that users recognise and abide by the legal requirements associated with these rights.

- Users may download and print one copy of any publication from the public portal for the purpose of private study or research.
- You may not further distribute the material or use it for any profit-making activity or commercial gain
- You may freely distribute the URL identifying the publication in the public portal

If you believe that this document breaches copyright please contact us providing details, and we will remove access to the work immediately and investigate your claim.

[Click here to view linked References](#)

Smearred Crack Modelling Approach for Corrosion- induced Concrete Damage

Anna Emilie A. Thybo

Alexander Michel

Henrik Stang

Department of Civil Engineering

Technical University of Denmark

Brovej, Building 118

2800 Kgs. Lyngby

Denmark

Phone: +45 2367 9969

Fax: +45 4588 3282

aeth@byg.dtu.dk

www.byg.dtu.dk

1 **Abstract**
2

3 In this paper a smeared crack modelling approach is used to simulate corrosion-induced damage in
4 reinforced concrete. The presented modelling approach utilizes a thermal analogy to mimic the
5 expansive nature of solid corrosion products, while taking into account the penetration of corrosion
6 products into the surrounding concrete, non-uniform precipitation of corrosion products, and creep.
7 To demonstrate the applicability of the presented modelling approach, numerical predictions in
8 terms of corrosion-induced deformations as well as formation and propagation of micro- and
9 macrocracks were compared to experimental data obtained by digital image correlation and
10 published in the literature. Excellent agreements between experimentally observed and numerically
11 predicted crack patterns at the micro and macro scale indicate the capability of the modelling
12 approach to accurately capture corrosion-induced damage phenomena in reinforced concrete.
13 Moreover, good agreements were also found between experimental and numerical data for
14 corrosion-induced deformations along the circumference of the reinforcement.
15
16
17
18
19
20

21 **Keywords:** Concrete cracking, Smeared crack modelling approach, FEM, Corrosion
22
23
24
25
26
27
28
29
30
31
32
33
34
35
36
37
38
39
40
41
42
43
44
45
46
47
48
49
50
51
52
53
54
55
56
57
58
59
60
61
62
63
64
65

1 Introduction

Along with globalisation, increase in population, and streamlining of transportation the demand for new infrastructures and, in general, the demand for sustainability of structures is expanding and, thereby, having a great effect on socio-economics. Understanding of structural performance as well as material behaviour is, therefore, of great importance and research within these fields has grown during the last decades (Andrade et al. 1993; Cabrera 1996; Molina et al. 1993; Alonso et al. 1998; Noghabai 1999; Solgaard et al. 2013; Michel et al. 2013).

A leading deterioration mechanism, in reinforced concrete structures, is corrosion (Rendell et al. 2002), which may cause debonding/delamination in the concrete/reinforcement interface, cracking in cover layer, and decrease in durability due to corrosion of steel. Several studies have focused on modelling corrosion-induced damage leading to a variety of modelling approaches, e.g. finite element (FE) based (Biondini and Vergani 2012; Solgaard 2013) and analytical (Bazant 1979; Liu and Weyers 1998; Chernin et al. 2010; Bohner E. 2010). Recent studies (Pease et al. 2012; Michel et al. 2013) have shown that corrosion products precipitate non-uniformly (even under accelerated conditions applying direct current) and penetrate into the surrounding concrete, which may have an influence on state-of-the-art FE modelling approaches dealing with corrosion-induced concrete damage.

Within this paper a FE modelling approach based on a discrete crack modelling that includes the penetration of corrosion products into the surrounding concrete (Michel et al. 2013) is further developed. The development includes the formulation of corrosion-induced concrete damage within a smeared crack modelling approach, which takes into account the penetration of corrosion products into the available pore space surrounding the reinforcement, non-uniform precipitation of corrosion products, and creep. The developed smeared crack modelling approach was then used to investigate the influence of the penetration of corrosion products into the surrounding concrete and the elastic modulus of corrosion products on corrosion-induced concrete damage. Finally, numerical results of the smeared crack modelling approach, i.e. modelled crack patterns, deformations near the concrete/reinforcement interface, and surface crack width, were compared to experimental observations obtained from accelerated corrosion experiments and data provided in the literature.

2 Introduction to corrosion-induced crack modelling

Once corrosion is initiated, electrochemical half-cell reactions are taking place along the reinforcement surface. The ionic reaction products of those half-cell reactions may further react and form solid corrosion products in the vicinity of the reinforcement. The type of corrosion products formed depends on the thermodynamic conditions present in the vicinity of the reinforcement (Küter et al. 2008). Apart from solid corrosion products, soluble iron-chloride complexes (also referred to as green rust) may form in an oxygen-deprived environment in which chlorides are present (Küter et al. 2008; Koleva et al. 2006). Such soluble iron-chloride complexes may not necessarily form in the vicinity of the reinforcement surface, as shown e.g. in Küter et al. (2008). However, independent of the type of iron oxides formed as a result of active corrosion, iron oxides occupy a larger volume than the initial iron that is consumed during the corrosion reaction; see e.g. Alonso et al. (1998). The increased volume of corrosion products causes tensile stresses in the

1 surrounding concrete and may lead to concrete cracking, spalling, or delamination, if the tensile
2 capacity of the concrete is exceeded.

3
4 To model the expansive nature of corrosion products, a thermal analogy may be used as shown in
5 Fig. 1. To mimic the increased volume of corrosion products, a ‘fictitious’ thermal load is applied to
6 the corroded reinforcement section. Basic geometrical considerations and finite element method
7 load application are illustrated in Fig. 1. The thickness of the corroded reinforcement section, $X(t)$,
8 may be determined using Faraday’s law, which describes the reduction in reinforcement radius due
9 to corrosion:
10

$$11 \quad X(t) = \frac{M i_{corr} \Delta t}{z F \rho} \quad (1)$$

12
13 M is the molar mass of the metal [g/mol], i_{corr} the corrosion current density [A/mm²], Δt the
14 duration of current application [s], z the anodic reaction valence [-], F Faraday’s constant [96485
15 As/mol] and ρ the density of the metal [g/mm³].

16 The thickness of the free expanding corrosion products can be expressed as (see e.g. Fig. 5):

$$17 \quad \Delta R_0 = R_2 - R_0 \quad (2)$$

18 Based on this, a ‘fictitious’ thermal load is applied to the corroded reinforcement section accounting
19 for the expansion of corrosion products:

$$20 \quad \Delta R_0 = X(t) \eta_{lin} = (R_0 - R_1) \eta_{lin} \quad (3)$$

21 where η_{lin} is the linear expansion coefficient [-] depending on the type of corrosion products formed
22 and described by a ‘fictitious’ thermal expansion coefficient, α [K⁻¹], and a corresponding
23 temperature increment, ΔT [K]. Assuming a constant coefficient of thermal expansion, α , the
24 applied temperature increment, ΔT , represents then the type of solid corrosion product. Assuming
25 further isotropic material properties of the corrosion products, the linear expansion coefficient may
26 be obtained as one third of the volume expansion coefficient:

$$27 \quad \eta_{lin} = \alpha \Delta T \quad (4)$$

28 **3 Discrete Crack Modelling Approach**

29 The foundation for the smeared crack modelling approach developed in this study is a FE based
30 modelling approach in which corrosion-induced concrete damage is simulated by means of a
31 discrete crack modelling approach (Michel et al. 2010; Solgaard 2013; Pease et al. 2012; Michel et
32 al. 2013).

33 In general, five distinct regions (concrete, reinforcement, corrosion layer, and a cracking and
34 debonding domain) form the modelled system, which simulates corrosion-induced cracking. In the
35 model, uniform corrosion was assumed along the length and along the circumference of the
36 reinforcement, for which a 2D plain strain formulation may be used. Cracking of the cementitious
37 matrix was considered along a predefined crack path including delamination at the
38 concrete/reinforcement interface, the former was modelled according to mode-I fracture and the
39 latter was modelled according to mixed-mode (combined modes I and II) fracture. The initial model
40
41
42
43
44
45
46
47
48
49
50
51
52
53
54
55
56
57
58
59
60
61
62
63
64
65

1 further assumed corrosion products form exclusively at the concrete/reinforcement interface. The
2 penetration of corrosion products, non-uniform precipitation of corrosion products, and creep were
3 not accounted for in the initial modelling approach presented in (Michel et al. 2010; Solgaard 2013).
4 The implementation of these reinforcement corrosion related phenomena within a smeared crack
5 modelling approach, are outline in the following sections.
6
7
8
9

10 **4 Smeared Crack Modelling Approach**

11 To overcome the limitations of the discrete crack modelling approach, in particular, the predefined
12 crack path and direction of a single corrosion-induced crack, the model was further developed
13 within a smeared crack modelling approach. However, the formulation of smeared crack approaches
14 in terms of continuous stress-strain relations (for a discontinuous phenomenon such as a corrosion-
15 induced crack) is associated with drawbacks when dealing with time-dependent problems such as
16 reinforcement corrosion. As, the nucleation of one or more corrosion-induced cracks leads to a
17 deterioration of the current stiffness and strength of the concrete domain, subsequent stress and
18 strain distribution depend on the stress and strain history (referred to as history dependency in the
19 present paper).

20 In this study, the commercial finite element program TNO DIANA was used to simulate crack
21 initiation and propagation using a smeared crack modelling approach. Within the model a multi-
22 directional fixed cracking (MDFC) model was used, which can be combined with time dependent
23 material models, such as e.g. creep. The MDFC model describes cracking using properties
24 regarding tension cut-off, shear retention, and tension softening. In the present study linear tension
25 cut-off was chosen viz. cracking occurs when the major principal tensile stress is larger than the
26 minimum of either tensile strength or a ratio between the tensile and compressive strength.
27 Following the previously developed discrete cracking approach, the shear modulus after cracking
28 was kept constant during simulation and multi-linear softening relations (adopted from Skocek
29 (2010)) are used to describe tension softening. A standard Newton-Raphson method with an energy
30 convergence criterion was used to obtain a solution of the nonlinear problem.

31 The implementation of penetration of corrosion products into the available pore space of the
32 cementitious matrix surrounding the reinforcement, non-uniform precipitation of corrosion products,
33 and creep within the smeared crack modelling approach is provided in the following sections.
34
35
36
37
38
39

40 **4.1 Penetration and non-uniform precipitation of corrosion products and creep**

41 Results of several experimental investigations described in the literature e.g. (Liu & Weyers 1998;
42 Val et al. 2009; Michel et al. 2011; Pease et al. 2012) indicate both the penetration of corrosion
43 products into the surrounding concrete and non-uniform precipitation of the corrosion products. The
44 penetration of corrosion products into the available pore space of the cementitious matrix
45 surrounding the reinforcement can be attributed to the porous nature of concrete, which allows
46 precipitation of corrosion products to a certain degree without inducing tensile stresses in the
47 concrete. Based on these observations (Michel et al. 2011), penetration and non-uniform
48 precipitation of corrosion products and the effect of creep was implemented in a FE based discrete
49
50
51
52
53
54
55
56
57
58
59
60
61
62
63
64
65

cracking modelling approach e.g. (Pease et al. 2012; Michel et al. 2013; Thybo et al. 2013), which can be adapted for smeared crack modelling approach.

4.1.1 Penetration of corrosion products

With the help of x-ray attenuation and digital image correlation measurements (Michel et al. 2011; Pease et al. 2012) were able to directly observe the penetration of corrosion products into the cementitious matrix surrounding the reinforcement reducing the effect of corrosion-induced expansion and, thereby, delaying the stress formation and initiation of cracking. Based on these observations, a conceptual approach to account for the penetration of corrosion products into the available pore space of cementitious material surrounding reinforcement was developed and presented in Michel et al. (2013). It is assumed that a corrosion accommodating region (CAR) around the reinforcement exists, initially denoted CAR_0 , which delays stress formation while filling with corrosion products. Once this initial CAR_0 is filled with corrosion products, tensile stresses in the surrounding cementitious material increase and potentially lead to the formation of microcracks. These microcracks allow solid corrosion products to penetrate additional pore spaces and further delay corrosion-induced stresses. At some point a maximum size of the CAR , denoted as CAR_{MAX} , is reached. No corrosion products can penetrate the matrix of the cementitious material beyond that point and all additionally formed corrosion products will introduce tensile stresses and potentially lead to the formation of a macrocrack.

The relationship between CAR , CAR_0 , and CAR_{MAX} was described in Michel et al. (2013):

$$CAR = CAR_0 + (CAR_{MAX} - CAR_0)\kappa \quad (5)$$

κ is a dimensionless coefficient describing the change in connectivity of accessible pore space inside the CAR [-] and is assumed to vary between 0 and 1 according to:

$$\kappa = 0 \quad \text{if } V_{cp} \leq V_{cp,min}$$

$$\kappa = \frac{V_{cp} - V_{cp,min}}{(V_{cp,max} - V_{cp,min})^{fp1}} \quad \text{if } V_{cp,min} < V_{cp} \leq V_{cp,max} \quad (6)$$

$$\kappa = 1 \quad \text{if } V_{cp} > V_{cp,max}$$

where V_{cp} is the expanded volume of corrosion products [mm^3], $V_{cp,min}$ is the minimum volume of corrosion products [mm^3] (Eq. 7) and $V_{cp,max}$ the maximum volume of corrosion products that can be accommodated in the CAR [mm^3] (Eq. 8), and $fp1$ a fitting parameter set to 1 [-].

The values of t in Eq. 7 and 8 are based on experimental observations from x-ray described in (Pease et al. 2012).

$$V_{cp,min} = 3\Delta T\pi l_A \left(R^2 - (R - X(t = 1.5))^2 \right) \quad (7)$$

$$V_{cp,max} = 3\Delta T\pi l_A \left(R^2 - (R - X(t = 5))^2 \right) \quad (8)$$

(Pease et al. 2012) introduced an adjusted temperature increment, ΔT_{CAR} , instead of ΔT (see Eq. 4) to account for the penetration of corrosion products.

$$\Delta T_{CAR} = \lambda_{CAR} \Delta T \quad (9)$$

λ_{CAR} describes the partial penetration of corrosion products [-] into the accessible (pore) space of the cementitious matrix and is defined as follows:

$$\lambda_{CAR} = \left(\frac{V_{cp}}{V_{CAR}} \right)^n \quad \text{if } V_{cp} < V_{CAR} \quad (10)$$

$$\lambda_{CAR} = 1 \quad \text{if } V_{cp} \geq V_{CAR}$$

where n is an empirical parameter discussed in (Pease et al. 2012) [-] and V_{CAR} the volume of the CAR [mm³]. The volume of the CAR is depending on the porosity and accessible volume of the concrete matrix:

$$V_{CAR} = \varphi V_{CM} \quad (11)$$

where φ is the capillary porosity of the concrete material [-], V_{CM} the accessible volume of concrete [mm³] depending on the size of CAR, see Eq. 5, the radius of the reinforcement, R [mm], and the length of the reinforcement which is corroding, l_A [mm].

$$V_{CM} = \pi l_A ((R + CAR)^2 - R^2) \quad (12)$$

4.1.2 Non-uniform precipitation of corrosion products

Among others, (Michel et al. 2012; Pease et al. 2012; Pease et al. 2012) observed that the precipitation of corrosion products was non-uniform along the circumference of the reinforcement although an impressed current was used to enhance the corrosion process. To account for the non-uniform precipitation of corrosion products within a discrete crack modelling approach, a corrosion current density vector, \mathbf{i}_{corr} , was introduced in Thybo et al. (2013). By varying the corrosion current density along the circumference of the reinforcement, see Fig. 1, different degrees of reinforcement corrosion were generated i.e. the reduction in reinforcement radius (as well as the partial penetration coefficient (Eq. 10) and the adjusted temperature increment (Eq. 9) depend on both time and location. Introducing \mathbf{i}_{corr} Eq. 1, 3, and 4 are replaced by Eq. 13, 14, and 15, respectively. A detailed explanation of the non-uniform precipitation of corrosion products is presented in Gebreyouhannes and Maekawa (2016) where the variation is explained as the result of the variation in the diffusion properties in the surrounding concrete resulting in a varying penetration of corrosion products into the concrete along the interface and thus resulting in varying stresses, deformations and consequently varying conditions for the corrosion process.

$$X(t) = R_0 - R_1 = \frac{M \mathbf{i}_{corr} \Delta t}{(\epsilon F \rho)} \quad (13)$$

$$\eta_{lin}(R_0 - R_1) = R_2 - R_0 \quad (14)$$

$$\eta_{lin} = \alpha \Delta T \quad (15)$$

4.1.3 Creep

To account for creep within the FE based smeared crack modelling approach, an effective modulus of elasticity for concrete was used according to Eurocode (2008), see Eq. 16. The implementation of creep was based on the assumption that the models concerning creep in larger volumes of concrete are also applicable for the volume size considered in the present study.

$$E_{c,eff} = \frac{E_c}{1 + \varphi(t_{age}, t_0)} \quad (16)$$

Where $E_{c,eff}$ is the effective modulus of elasticity [MPa], E_c the tangent modulus of elasticity [MPa], $\varphi(t_{age}, t_0)$ the creep coefficient [-], t_{age} the age of the concrete [days] and t_0 the time at loading [days].

4.2 Convergence of mesh

To investigate the impact of number of elements in the concrete domain and the number of corroding steel elements along the circumference of the reinforcement on corrosion-induced crack widths, a convergence analysis was carried out. Fig. 2 illustrates a plot of the mesh highlighting the concrete, steel, and corroding steel domain. Three noded triangular plane stress elements were used to discretize both the concrete and steel domain, while four-noded quadrilateral plane stress elements were used to discretize the corroding steel domain. A zoom of the corroding steel domain is illustrated underlining that the corroding steel domain consists of several elements in the radial direction. The number of elements in radial direction depends on the number of ‘time steps’ selected during the simulation (see section 4.3).

For the convergence analysis the number of elements within the concrete domain was varied between approximately 4000 and 49000 elements. Results of the analysis for a thickness of the corroding steel domain of 0.035 mm are presented in Fig. 3 and have been normalised with respect to the results for 49082 elements. A maximum deviation of approximately 2 % is observed when increasing the number of elements from around 30000 to 49082. Thus, it was concluded that approximately 30000 elements in the concrete domain are sufficient to model corrosion-induced cracking and it is actually possible to reduce the number of elements to optimize computational time without compromising accuracy of the simulations significantly. For the convergence analysis of the number of elements along the circumference of the reinforcement, 24, 36, 48, 148, and 192 elements were chosen to discretize the corroding steel domain. Results of the analysis are illustrated in Fig. 4 for a thickness of the corroding steel domain of 0.035 mm and were normalised with respect to the results for 192 elements. It is seen that between 48 and 192 elements a deviation of less than 2% is observed. Therefore, it was concluded that 48 elements along the circumference of the reinforcement are sufficient for modelling corrosion-induced cracking without compromising accuracy. The influence of number of corroding steel elements in radial direction and the effect of number of elements in the steel domain was not investigated.

4.3 History dependency

In the following the ‘history dependency’ of the developed smeared crack modelling approach was investigated comparing initiation time and surface crack widths varying the number of intermediate ‘load steps’. In the following the number of intermediate ‘load steps’ is referred to as ‘time steps’. The applied number of ‘time steps’ for the various simulations, is schematized in Table 4.1, along

with results of surface crack width, which are also visualised in Fig. 5. The input parameters for the various simulations are given in Table 4.2.

Table 4.1 Overview of time-to crack initiation and surface crack width after 20 days for varying numbers of ‘time steps’.

No. of ‘time steps’	Time to crack initiation [days]	Deviation of time at first given crack value [%]	Deviation of surface crack width after 20 days [%]
1	-	-	29.1
3	12*	20.0	5.4
5	12*	20.0	5.1
20	11*	10.0	2.5
40	10.5	5.0	2.0
80	10.25	2.5	1.0
200	10	0	0

*In Fig. 9 it is seen that the crack initiates earlier, however this is the first given value due to the low number of ‘time steps’.

Table 4.2 Input parameters for smeared crack modelling approach to investigate varying number of ‘time steps’.

	Parameter	Value	Dimension
Length	L	23	mm
Width	W	100	mm
Height	H	100	mm
Cover layer	C	45	mm
Reinforcement diameter	D	10	mm
Water-to-cement ratio	w/c	0.5	-
Concrete compressive strength	f_{cm}	45	MPa
Tangent modulus of elasticity - concrete	E_c	36.272	GPa
Shear stiffness	G_c	10	GPa
Poisson ratio - concrete	μ_c	0.2	-
Modulus of elasticity - steel	E_s	210	GPa
Poisson ratio - steel	μ_s	0.3	-
Modulus of elasticity - corrosion products	E_{corr}	2	GPa
Poisson ratio - corrosion products	μ_{corr}	0.2	-
Relative humidity	RH	65	%
Molar mass – steel	M_{Fe}	55.845	g/mol
Valence	z	2	-
Steel density	ρ_{steel}	7.86	g/cm ³
Faraday’s constant	F	96485	A·s/mol
Mean corrosion current density	i_{corr_mean}	0.0001	A/cm ²
Min. corrosion accommodating region	CAR_0	0.14	mm
Max. corrosion accommodating region	CAR_{MAX}	0.28	mm
Min. volume of corrosion products in CAR	$V_{cp,min}$	7.15	mm ³
Max. volume of corrosion products in CAR	$V_{cp,max}$	23.8	mm ³
Linear expansion coefficient	η_{lin}	0.7	-
Fictitious thermal expansion coefficient	α	1	-

From the results presented in Fig. 5 it can be seen that both surface crack width and time-to crack initiation depend on the number of ‘time steps’ (deformation history) in the smeared crack modelling approach. In general, it is observed that with decreasing number of ‘time steps’ insufficient and incorrect information on time-to crack initiation, crack width development over time, and final crack width are obtained. More realistic crack width development and final crack width are obtained with the modelling approach, when more than three ‘time steps’ are used. However, larger deviations with respect to the time-to crack initiation are still observed for an insufficient number of ‘time steps’. This relation is highlighted in Table 4.1, where it can be observed that the final surface crack width (surface crack width at 20 days) is less affected by the

1 number of ‘time steps’ compared to the time-to crack initiation. The results presented in Table 4.1
2 indicate that the number of ‘time steps’ should be based on desired accuracy with respect to crack
3 width development and time-to crack initiation. In order to minimise computational time and at the
4 same time maintain an acceptable accuracy it was chosen to run simulations in the following with
5 40 ‘time steps’. For this number of ‘time steps’, approximately 5% and 2 % deviation with respect
6 to time-to crack and final surface crack width are expected, respectively (compared to 200 ‘time
7 steps’).
8
9
10

11 **5 Comparison between experimental and numerical results**

12 To demonstrate the applicability of the developed FE based smeared crack modelling approach
13 (including the penetration of solid corrosion products into the cementitious matrix, non-uniform
14 precipitation of corrosion products, and creep) to predict corrosion-induced deformations and crack
15 formation, numerical simulations were compared to two experimental studies: (1) results of digital
16 image correlation (DIC) measurements presented in (Pease et al. 2012; Michel et al. 2013) and (2)
17 experimental observations from Vu et al. (2005). In addition, results of the previously developed
18 discrete crack modelling approach were also compared to predictions of the smeared crack
19 modelling approach.
20
21
22
23
24
25
26

27 **5.1 Experimental investigations**

28 Pease et al. (2012) used digital image correlation (DIC) measurements to study the formation of
29 corrosion products and corrosion-induced deformation in reinforced mortar specimens ($w/c = 0.5$)
30 under accelerated corrosion conditions. Each specimen was 23 mm \times 100 mm \times 100 mm and a
31 smooth 10 mm steel rod was placed in the centre as reinforcement. During the experiments, the
32 specimens were placed in an acrylic pond containing tap water and a volumetric flask was used to
33 maintain the water level at about 1 cm below the reinforcement. To enhance the reinforcement
34 corrosion process, a DC regulator was used to impress a constant electrical current ($100 \mu\text{A}/\text{cm}^2$)
35 through the counter electrode (activated titanium mesh). Deformations were measured using DIC
36 technique allowing for crack measurements on the specimen surface, see e.g. Pease et al. (2012).
37
38
39
40

41 For the DIC measurement technique, digital images were repeatedly captured at 10 minute intervals
42 using a Nikon D3X 24.5 megapixel (6048 \times 4032 pixel) camera body with a 60 mm focal length
43 macro lens (AF-S Micro Nikkor 60mm f/2.8G ED). Prior to initiation of accelerated corrosion
44 testing, three images were captured of the specimen surface, with a fourth image including a scale.
45 The lens was placed 60 mm from the specimen surface, resulting in images with dimensions of
46 approximately 31 \times 41 mm², with each pixel representing 7.8 \times 7.8 μm^2 of physical space (Pease et al.
47 2012).
48
49
50

51 Captured images were input into a commercially available software package (GOM 2009), which
52 utilizes a previously applied stochastic speckle pattern to identify unique regions, called facets, on
53 the specimen surface at each measurement time. The software tracks the movements of the facets
54 and utilizes standard DIC techniques to compute deformations of the specimen surface. Additional
55 information on the hardware used and the DIC technique is available in Pereira et al. (2011) and
56 Pease et al. (2006), respectively Pease et al. (2012).
57
58
59
60
61
62
63
64
65

1 In addition, a trial test, to assess DIC measurement accuracy, was conducted by placing two mortar
2 prisms side-by-side with flat faces touching each other. Prisms were fixed to a micrometer setup
3 with 1 μm gradations with one prism stationary and the second moving with controlled distances.
4 Two 2.5 mm extensometers were used to provide comparative displacement measurements
5 between the fixed and moving mortar prisms. The moving prism was translated by the micrometer
6 setup to varying locations. At each location 3 digital images and 20 extensometer measurements
7 were recorded. A maximum difference of 0.29 μm was found for deformations from 0 to 26.2 μm
8 comparing results of DIC measurement technique and extensometer measurements Pease et al.
9 (2012).
10

11 The accelerated corrosion test was stopped when the first macro-crack near the
12 concrete/reinforcement interface was observed. For more information about preparation of the
13 specimens, test setup, and measurement technique reference is made to Pease et al. (2012).
14

15 To fit the experimental observations, a vector describing the non-uniform corrosion along the
16 circumference of the reinforcement was defined. The non-uniform corrosion current density along
17 the circumference of the reinforcement was estimated using the experimental deformations after
18 three days of accelerated corrosion as a starting point. A comparison between measured
19 deformations after three days of accelerated corrosion and applied corrosion current density along
20 the circumference of the reinforcement is illustrated in Fig. 6. The average corrosion current density
21 was 100 $\mu\text{A}/\text{cm}^2$ and local variations may be attributed to factors such as reinforcement surface
22 condition and moisture distribution around the reinforcement. In addition, the concrete tensile
23 strength, f_{cm} , was chosen to be 4.5 [MPa] and the non-physical modelling parameters $fp1$ and n
24 were set to 2.2 and 1.8, respectively. An overview of the input parameters for the smeared crack
25 modelling approach is given in Table 4.2.
26
27
28
29
30
31
32
33

34 Similar to Pease et al. (2012), Vu et al. (2005) conducted accelerated corrosion tests to study the
35 formation of corrosion-induced concrete cover cracks. Reinforced concrete slabs with w/c of 0.45,
36 0.5, and 0.58 were submersed in 5% sodium chloride (NaCl) solution and tested under accelerated
37 conditions applying a constant current density of 100 $\mu\text{A}/\text{cm}^2$. Corrosion-induced cracks were
38 measured using a combination of magnifying glass and displacement transducers. Testing was
39 stopped when a crack width of 1.0 - 1.5 mm at the concrete surface was measured. More detailed
40 information on specimen preparation, material properties, and experimental setup are provided in
41 Vu et al. (2005).
42

43 To simulated the experimental observations described in Vu et al. (2005), i.e. time-to crack
44 initiation and surface crack width, input parameters for the model described in Table 5.1 were used.
45 In addition, the concrete tensile strength compressive strength and volume expansion coefficient
46 were set to 4.16 MPa, 43 MPa and 2,94, respectively, as provided in Vu et al. (2005). Furthermore,
47 the non-physical modelling parameters $fp1$ and n were set to 2.2 and 1.8, respectively. Further,
48 Poisson's ratio and elastic modulus of corrosion products were set to 0.2 and 2 GPa, respectively, as
49 e.g. provided in (Solgaard et al. 2013, Caré 2008).
50
51
52
53
54
55
56
57
58
59
60
61
62
63
64
65

Table 5.1 Input parameters for smeared crack modelling approach comparing to experimental data from Vu et al. (2005).

	Parameter	Value	Dimension
Length	L	1000	mm
Width	W	156	mm
Height	H	250	mm
Cover layer	C	50	mm
Reinforcement diameter	D	16	mm
Water-to-cement ratio	w/c	0.5	-
Tangent modulus of elasticity - concrete	E_c	36.272	GPa
Shear stiffness	G_c	10	GPa
Poisson ratio - concrete	μ_c	0.2	-
Modulus of elasticity - steel	E_s	210	GPa
Poisson ratio - steel	μ_s	0.3	-
Relative humidity	RH	65	%
Molar mass – steel	M_{Fe}	55.845	g/mol
Valence	z	2	-
Steel density	ρ_{steel}	7.86	g/cm ³
Faraday's constant	F	96485	A·s/mol
Mean corrosion current density	$i_{corr, mean}$	0.0001	A/cm ²
Min. corrosion accommodating region	CAR_0	0.14	mm
Max. corrosion accommodating region	CAR_{MAX}	0.22	mm
Min. volume of corrosion products in CAR	$V_{cp, min}$	2351	mm ³
Max. volume of corrosion products in CAR	$V_{cp, max}$	705	mm ³
Fictitious thermal expansion coefficient	α	1	-

5.2 Results and discussion

The ability of the presented smeared crack modelling approach is discussed with respect to three criteria: 1) corrosion-induced deformations near the concrete/reinforcement interface, 2) corrosion-induced crack patterns, and 3) time-to surface crack initiation and surface crack width. To quantify the ability of the model to simulate corrosion-induced deformations and cracks in the vicinity of the concrete/reinforcement interface, experimental results of digital image correlation measurements presented in Michel et al. (2013) were used. Numerical predictions of time-to surface crack initiation and surface crack width were compared to experimental data presented in Vu et al. (2005). Comparisons between experimentally observed corrosion-induced deformations along the circumference of the reinforcement and numerical predictions using the presented smeared crack modelling approach and the previously developed discrete crack modelling approach (Pease et al. 2012; Thybo et al. 2013) are presented in Fig. 8. Numerical and experimental results are given after three, six, and nine days of accelerated corrosion in polar coordinates (see also Fig.7). As can be seen from the results presented in Fig. 7, excellent agreement (with respect to shape and magnitude) between experimentally observed and numerically predicted corrosion-induced deformations is found for six and nine days of accelerated corrosion.

In addition, experimentally observed microcracks (by means of DIC) due to accelerated corrosion are illustrated in Fig. 8. DIC allows thereby for identification of cracks as zones with localized strain, i.e. areas in red and light blue in Fig. 8. Three corrosion-induced microcracks (with crack widths between approximately two and ten μm) and considerable damage along the circumference of the reinforcement can be identified in Fig. 8. The microcracks formed at the reinforcement, extend around 10 to 15 mm in the mortar, and propagated towards the surface over time. For comparison, the crack pattern obtained by the presented smeared crack modelling approach and previously developed discrete crack modelling approach is given in Fig. 10 and Fig. 9, respectively.

1 Similar crack pattern and corrosion-induced damage along the circumference of the reinforcement
2 are obtained with the smeared crack modelling approach, while only one corrosion-induced crack is
3 formed along the predefined crack path in the discrete crack modelling approach. Furthermore,
4 extensive damage along the circumference of the reinforcement, in particular on the right side, and
5 micro-cracking are observed in the smeared crack modelling approach (see Fig. 10), which is not
6 captured by the discrete crack modelling approach (see Fig. 9). In particular, three microcracks,
7 which formed at the reinforcement and propagate towards the surface, can be observed in Fig. 10.
8 While the direction of the microcracks is not completely in agreement with the experimental
9 observations, the extent of the microcracks is in good agreement with numerical predictions of the
10 smeared crack modelling approach. However, it should be noted that results of the presented DIC
11 measurement technique only provide information on corrosion-induced deformations and cracking
12 on the specimen surface, i.e. details on corrosion-induced deformations and cracking within the
13 specimen cannot be obtained with DIC. For additional validation of the presented modelling
14 approach (accelerated) corrosion test may be undertaken in e.g. a μ -CT allowing for the observation
15 of corrosion-induced deformations and cracking within the specimen.
16
17
18
19
20
21
22

23 Finally, Fig. 11 illustrates a comparison of experimentally observed corrosion-induced surface
24 crack width (Vu et al. 2005) and numerical predictions with the presented smeared crack modelling
25 approach (taking into account and neglecting the penetration of corrosion products into the
26 surrounding concrete). It can be clearly seen from the presented results that the model is able to
27 accurately capture the time-to crack initiation when the penetration of corrosion products into the
28 surrounding concrete is taken into account. Larger deviations between experimental observations
29 and numerical predictions with respect to the time-to crack initiation are found when the penetration
30 of corrosion products into the surrounding concrete is neglected; please note the logarithmic time
31 scale in Fig. 11. While the time-to crack initiation is accurately captured with the presented smeared
32 crack modelling approach, some deviations are found between experimentally observed and
33 numerically predicted surface crack opening. Those deviations maybe be explained due to lacking
34 information on fracture mechanical properties, in particular, the softening behaviour of the concrete
35 material, as only the tensile strength was provided in Vu et al. (2005).
36
37
38
39
40
41

42 *5.2.1 Influence of elastic modulus of corrosion products*

43 Deterioration models, such as the presented smeared crack modelling approach, developed to better
44 understand corrosion-induced cracking processes in reinforced concrete, have highlighted a key
45 parameter in the cracking process - namely, the elastic properties of reinforcement corrosion
46 products (Molina et al. 1993, Solgaard 2013). Citing a lack of experimental observations (Molina et
47 al. 1993) assumed water comprised the majority of corrosion products and therefore used water's
48 elastic properties (2 GPa elastic modulus, 0.5 Poisson's ratio) to characterize the mechanical
49 properties of corrosion products. Direct measurement of elastic properties of corrosion products is
50 complicated due to the materials' stratified lamina nature. However, recently works attempted to
51 quantify properties of reinforcement corrosion products (Ouglova et al. 2006; Caré et al. 2008;
52 Pease et al. 2012). Generally it was concluded that the elastic properties depend on the type and
53 conditions under which corrosion products are formed e.g. degree of confinement, supply of oxygen,
54
55
56
57
58
59
60
61
62
63
64
65

1 etc. In Pease et al. (2012) a discrete crack modelling approach was used to compare experimental
2 observations of crack widths near the concrete/reinforcement interface (obtained by means of digital
3 image correlation) with numerical predictions. Within their studies, (Pease et al. 2012) found that
4 elastic properties of the corrosion products between 2 and 20 GPa provided the best fit for the
5 experimental data. Similar to Pease et al. (2012), the smeared crack modelling approach presented
6 in this study was used to investigate the influence of the elastic properties of corrosion products on
7 the time-to corrosion-induced cracking and development of surface cracks comparing numerical
8 predictions and experimental observations from Vu et al. (2005), see Fig. 11. Elastic properties of
9 corrosion products were thereby varied between 0.2 and 200 GPa.

10 Fig. 12 illustrates numerical results of the smeared crack modelling approach and experimental
11 results for varying elastic properties of the corrosion products. From the presented results in Fig. 12,
12 it can be seen that the elastic properties of the corrosion products affect both time-to corrosion-
13 induced cracking and development of surface crack width. However, the impact on the time-to
14 corrosion-induced cracking is lower than the influence on the development of the surface crack
15 width, in particular for elastic properties in the range of 0.2 to 20 GPa. Significant changes in the
16 time-to crack initiation and development of surface crack width are observed for elastic properties
17 in the range of 200 GPa, in which case the smeared crack modelling approach considerably
18 overestimates the experimental observations both with respect to time-to crack initiation and
19 development of surface crack width.

20 **6 Summary and Conclusions**

21 In the present paper a finite element based smeared crack modelling approach was introduced to
22 simulate corrosion-induced concrete damage. The presented modelling approach utilizes a thermal
23 analogy to mimic the expansive nature of solid corrosion products and furthermore takes into
24 account the penetration of corrosion products into the surrounding concrete, non-uniform
25 precipitation of corrosion products, and creep. To demonstrate the applicability of the presented
26 modelling approach, numerical predictions in terms of corrosion-induced deformations as well as
27 formation and propagation of micro- and macrocracks were compared to experimental data obtained
28 by digital image correlation and published in the literature. From the presented studies using the
29 developed smeared crack modelling approach it may be concluded that:

- 30 1 The time-to crack initiation depends on the number of ‘time steps’ (deformation history) in the
31 smeared crack modelling approach. In general, it is observed that with decreasing number of
32 ‘time steps’ insufficient and incorrect information on time-to crack initiation, crack width
33 development over time, and final crack width are obtained. Preliminary modelling results
34 indicate that the chosen number of ‘time steps’ should be based on desired accuracy with
35 respect to crack width development and time-to crack initiation.
- 36 2 Excellent agreements between experimentally observed and numerically predicted crack
37 patterns at the micro and macro scale indicate the capability of the modelling approach to
38 accurately capture corrosion-induced damage phenomena in reinforced concrete. Moreover,
39 good agreements were also found between experimental and numerical data for corrosion-
40

1 induced deformations along the circumference of the reinforcement. In particular, the
2 assumption of non-uniform corrosion around the circumference of the reinforcement led to a
3 considerable improvement of numerical predictions concerning corrosion-induced deformations
4 in comparison to previously presented modelling approaches.
5

- 6
- 7 3 The penetration of corrosion products into the available pore space of the cementitious matrix
8 surrounding the reinforcement has a considerable effect on the time-to crack initiation. While in
9 the present study the effect was demonstrated for accelerated corrosion conditions, the influence
10 is even more pronounced under natural corrosion conditions, where corrosion current densities
11 in the range of approximately 0.1 to 1 $\mu\text{A}/\text{cm}^2$ can be expected. It should be noted that in the
12 present study homogeneous diffusion properties governing the penetration of corrosion products
13 into the concrete were applied, while a more detailed study (Gebreyouhannes and Maekawa
14 2016) applied inhomogeneous diffusion properties providing an underlying explanation for the
15 varying precipitation of corrosion properties along the circumference of the reinforcement.
16
 - 17 4 The elastic properties of the corrosion products affect both time-to corrosion-induced cracking
18 and development of surface crack width. However, the impact on the time-to corrosion-induced
19 cracking is lower than the influence on the development of the surface crack width, in particular
20 for elastic properties in the range of 0.2 to 20 GPa. Within the present study values for the
21 elastic modulus of corrosion products between 2.0 and 20.0 GPa provided most accurate fits to
22 experimental results both with respect to time-to crack initiation and development of surface
23 crack width.
24
25
26
27
28

29
30 Despite the good results found in the present study, future investigations should focus on improving
31 modelling considerations regarding among others 3D analyses including non-uniform corrosion
32 along the reinforcement as well as the inhomogeneous nature of concrete.
33
34

35 36 **7 Acknowledgements**

37
38 The authors gratefully acknowledge the financial support of the Danish Expert Centre for
39 Infrastructure Constructions. Further, the authors would like to thank Bradley J. Pease for
40 contributing with experimental data.
41
42
43
44

45 46 **Compliance with Ethical Standards**

47
48 The first author has received funding from the Danish Expert Centre for Infrastructure
49 Constructions. No grant number exists.
50

51 52 **Conflict of Interest Statement**

53
54 The authors declare that they have no conflict of interest.
55
56
57
58
59
60
61
62
63
64
65

References

- Alonso C, Andrade C, Rodriguez J, Diez JM (1998) Factors controlling cracking of concrete affected by reinforcement corrosion. *Materials and Structures* 45:435-441. doi: 10.1007/BF02480466
- Andrade C, Alonso C, Molina FJ (1993) Cover cracking as a function of bar corrosion: Part I- Experimental test. *Materials and Structures* 26:453-464. doi:10.1007/BF02472805
- Bazant ZP (1979) Physical Model for Steel Corrosion in Concrete Sea Structures - Theory. *Journal of the Structural Division-ASCE*, 105:1137-1153
- Biondini F, Vergani M (2012) Damage modeling and nonlinear analysis of concrete bridges under corrosion. In: *Proceedings of 6th International Conference on Bridge maintenance, safety and management (IABMAS)*, Lake Como
- Bohner E, Müller HS, Bröhl S (2010) Investigations on the mechanism of concrete cover cracking due to reinforcement corrosion. In: *Proceedings for FraMCoS-7—7th International Conference on Fracture Mechanics of Concrete and Concrete Structures*, Jeju
- Cabrera JG (1996) Deterioration of Concrete Due to Reinforcement Steel Corrosion. *Cement and Concrete Composites* 18: 47-59. doi:10.1016/0958-9465(95)00043-7
- Care S, Nguyen QT, L'Hostis V, Berthaud Y (2008). Mechanical properties of the rust layer induced by impressed current method in reinforced mortar. *Cement and Concrete Research* 38:1079-1091. doi:10.1016/j.cemconres.2008.03.016
- Chernin L, Val DV, Volokh KY (2010). Analytical modelling of concrete cover cracking caused by corrosion of reinforcement. *Materials and Structures* 43:543-556. doi: 10.1617/s11527-009-9510-2
- Concrete Structures, DS/S-19000 Eurocode (2008) Eurocode 2: Design of Concrete Structures - Part 1-1: General Rules and Rules for Buildings
- Gebreyouhannes E, Maekawa K (2016). Nonlinear Gel Migration in Cracked Concrete and Broken Symmetry of Corrosion Profiles. *Journal of Advanced Concrete Technology* 14:271-286. doi: 10.3151/jact.14.271
- GOM (2009) Aramis user manual – Software, Aramis v6.1 and higher. GOM Optical Measuring Techniques.
- Koleva DA, Hu J, Fraaij ALA, Stroeven P, Boshkov N, de Wit JHW (2006) Quantitative characterisation of steel/cement paste interface microstructure and corrosion phenomena in mortars suffering from chloride attack. *Corrosion Science* 48:4001-4019. doi: 10.1016/j.corsci.2006.03.003
- Küter A (2008) Management of Reinforcement Corrosion. Dissertation, Technical University of Denmark
- Liu Y, Weyers RE (1998) Modeling the Time-to-Corrosion Cracking in Chloride Contaminated Reinforced Concrete Structures. *ACI Materials Journal* 95:675-681.
- Michel A, Pease BJ, Geiker MR, Stang H, Olesen JF (2011) Monitoring reinforcement corrosion and corrosion-induced cracking using non-destructive x-ray attenuation measurements. *Cement and Concrete Research* 41:1085-1094. doi: 10.1016/j.cemconres.2011.06.006
- Michel A, Pease BJ, Peterova A, Geiker MR, Stang H, Thybo AEA (2013) Penetration of corrosion products and corrosion-induced cracking in reinforced cementitious materials:

1 experimental investigations and numerical simulations. *Cement and Concrete Composite* 47:75-86.
2 doi: 10.1016/j.cemconcomp.2013.04.011
3

4 Michel A, Pease BJ, Peterova A, Geiker MR (2012) Experimental determination of the
5 penetration depth of corrosion products and time to corrosion-induced cracking in reinforced
6 cement based materials. In: *Proceedings of International Congress on Durability of Concrete,*
7 *Trondheim*
8

9 Michel A, Solgaard AOS, Geiker MR, Stang H, Olesen JF (2010) Modeling Formation of
10 Cracks in Concrete Cover due to Reinforcement Corrosion. In: *Proceedings for FraMCos-7—7th*
11 *International Conference on Fracture Mechanics of Concrete and Concrete Structures, Jeju*
12

13 Molina FJ, Alonso C, Andrade C (1993) Cover cracking as a function of rebar corrosion: Part
14 2—Numerical model. *Materials and Structures* 26:532–548. doi 10.1007/BF02472864
15

16 Noghabai K. (1999) FE-Modelling of cover splitting due to corrosion by use of inner softening
17 band. *Materials and Structures* 32:486–491. doi: 10.1007/BF02481632
18

19 Ouglova A, Berthaud Y, Francois M, Foct F (2006). Mechanical properties of an iron oxide
20 formed by corrosion in reinforced concrete structures. *Corrosion Science*, 48:3988–4000. doi:
21 10.1016/j.corsci.2006.03.007
22

23 Pease BJ, Geiker MR, Stang H, Weiss WJ (2006) Photogrammetric Assessment of Flexure
24 Induced Cracking of Reinforced Concrete Beams under Service Loads. In: *Proceedings of the*
25 *Second International RILEM Symposium : Advances in Concrete through Science and Engineering,*
26 *Québec City*
27

28 Pease BJ, Michel A, Thybo AEA, Stang H (2012) Estimation of elastic modulus of
29 reinforcement corrosion products using inverse analysis of digital image correlation measurements
30 for input in corrosion-induced cracking model. In: *Proceedings of 6th International Conference on*
31 *Bridge maintenance, safety and management (IABMAS), Lake Como*
32

33 Pease BJ, Michel A, Stang H (2012) Quantifying movements of corrosion products in
34 reinforced concrete using x-ray attenuation measurements. In: *Proceedings for 2nd International*
35 *Conference on Microdurability, Amsterdam*
36

37 Pereira EB, Fischer G, Barros JA (2011) Image-based detection and analysis of crack
38 propagation in cementitious composites. In: *Proceedings of International RILEM Conference On*
39 *Advances In Construction Materials Through Science and Engineering, Hong Kong*
40

41 Rendell F, Jauberthie R, Grantham M (2002) *Deteriorated Concrete: Inspection and*
42 *Physicochemical Analysis.* Thomas Telford Ltd.
43

44 Skocek J (2010) *Fracture propagation in cementitious materials Multi-scale approach :*
45 *measurements and modeling.* Dissertation, Technical University of Denmark
46

47 Solgaard AOS (2013) *Corrosion of reinforcement bars in steel fibre reinforced concrete*
48 *structures.* Dissertation, Technical University of Denmark
49

50 Solgaard AOS, Michel A, Geiker MR, Stang H (2013). Concrete cover cracking due to uniform
51 reinforcement corrosion. *Materials and Structures* 46:1781-1799. doi: 10.1617/s11527-013-0016-6
52

53 Thybo AEA, Michel A, Stang H (2013) Modeling of Corrosion-induced Concrete Damage. In:
54 *Proceedings for FraMCos-8—8th International Conference on Fracture Mechanics of Concrete and*
55 *Concrete Structures, Toledo*
56
57
58
59
60
61
62
63
64
65

1 Val DV, Chernin L, Stewart MG (2009) Experimental and numerical investigation of
2 corrosion-induced cover cracking in reinforced concrete structures. *Journal of Structural*
3 *Engineering* 135:376–385. doi: 10.1061/(ASCE)0733-9445(2009)135:4(376)
4

5 Vu K., Stewart MG, Mullard J (2005). Corrosion-induced cracking: experimental data and
6 predictive models. *ACI Structural Journal* 102:719–726.
7

8 Zhao Y, Dai H, Ren H, Jin W (2012). Experimental study of the modulus of steel corrosion in a
9 concrete port. *Corrosion Science* 56:17–25. doi: 10.1016/j.corsci.2011.11.004
10
11
12
13
14
15
16
17
18
19
20
21
22
23
24
25
26
27
28
29
30
31
32
33
34
35
36
37
38
39
40
41
42
43
44
45
46
47
48
49
50
51
52
53
54
55
56
57
58
59
60
61
62
63
64
65

List of Figures

Fig. 1 Load application (left) and basic geometrical considerations to model non-uniform formation of corrosion products (right) in the smeared crack model, from Thybo et al. (2013)

Fig. 2 Plot of mesh

Fig. 3 Convergence plot of elements in concrete

Fig. 4 Convergence plot of elements along perimeter of reinforcement

Fig. 5 Modelled corrosion-induced surface crack widths for varying number of 'time steps'

Fig. 6 Measured deformations (solid line) along the circumference of the reinforcement after three days of accelerated corrosion and corresponding estimated non-uniform corrosion current density (dashed line)

Fig. 7 Comparison of corrosion-induced deformations measured by DIC with numerical results obtained from a previously developed discrete cracking modelling approach (Michel et al. 2013) and the presented smeared crack modelling approach assuming non-uniform corrosion

Fig. 8 Corrosion-induced cracks in reinforced specimens after nine days of accelerated corrosion, please note: only part of the test specimen is illustrated

Fig. 9 Modelled crack development using the discrete crack modelling approach

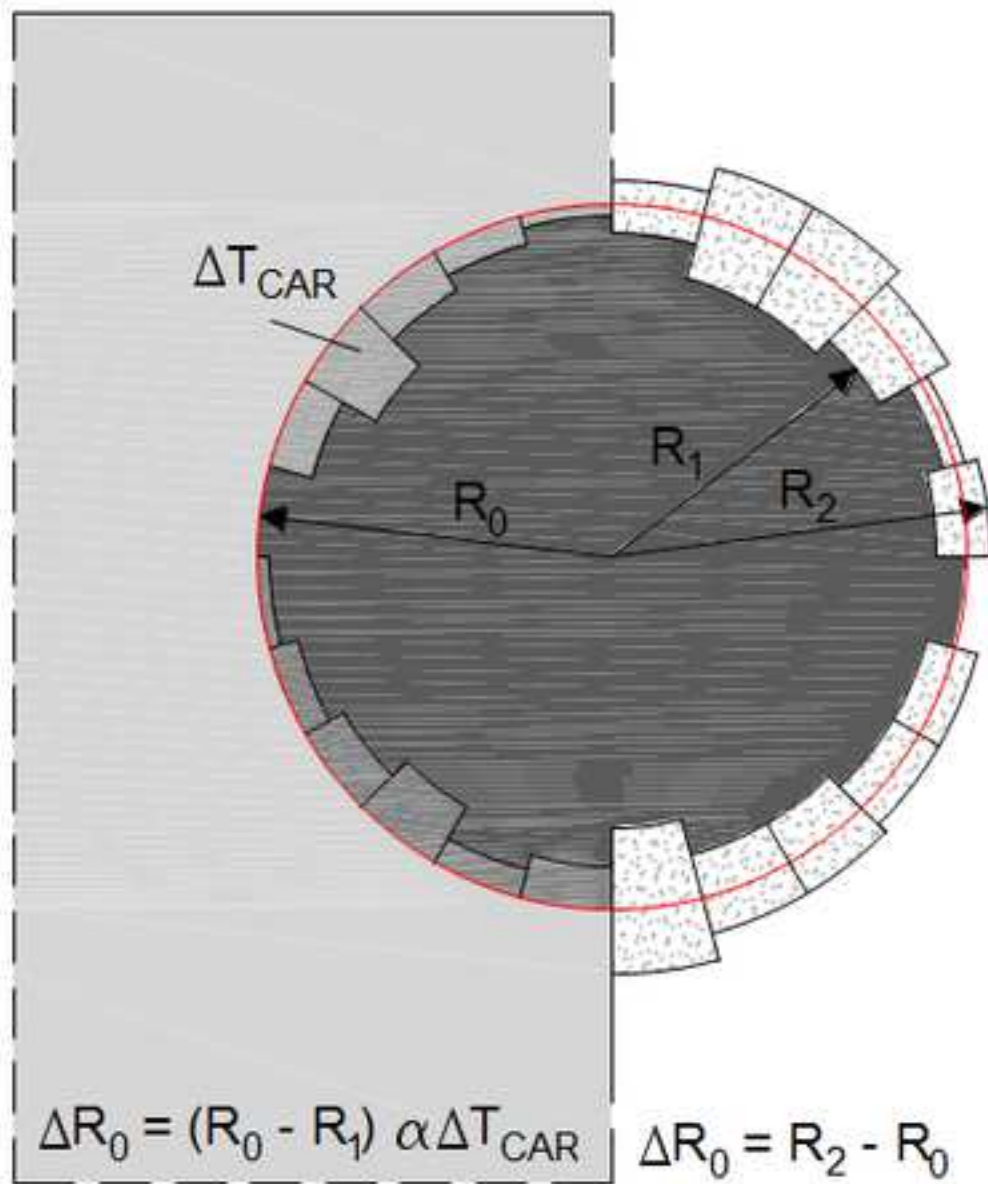
Fig. 10 Modelled crack development using the smeared crack modelling approach






Fig. 11 Comparison of corrosion-induced surface cracking presented in Vu et al. (2005) with numerical results applying the presented smeared crack modelling approach (with and without penetration of corrosion products into the surrounding concrete)

Fig. 12 Comparison of corrosion-induced surface crack widths for different elastic moduli of corrosion products using a smeared crack modelling approach

FEM model

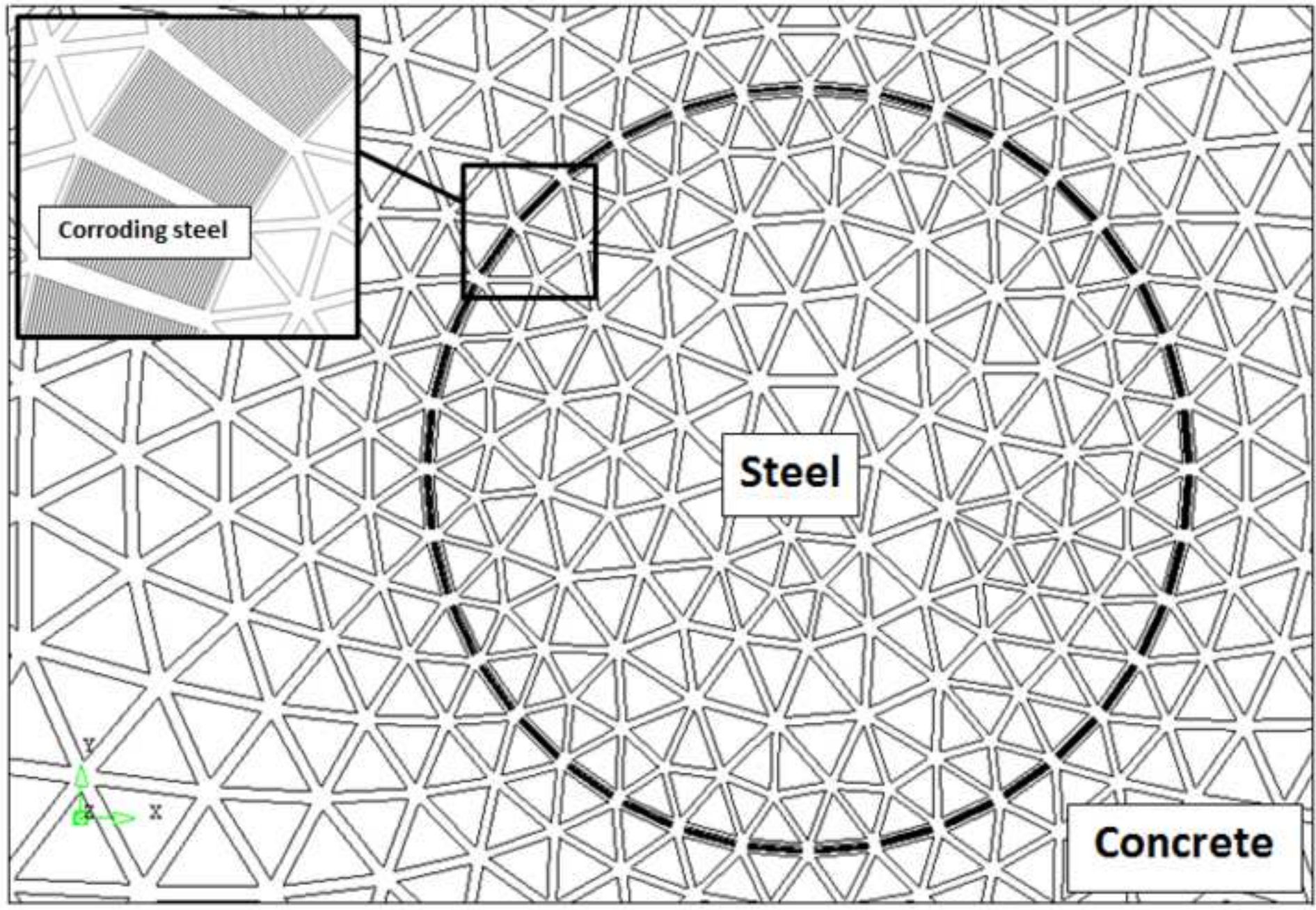
Geometrical considerations

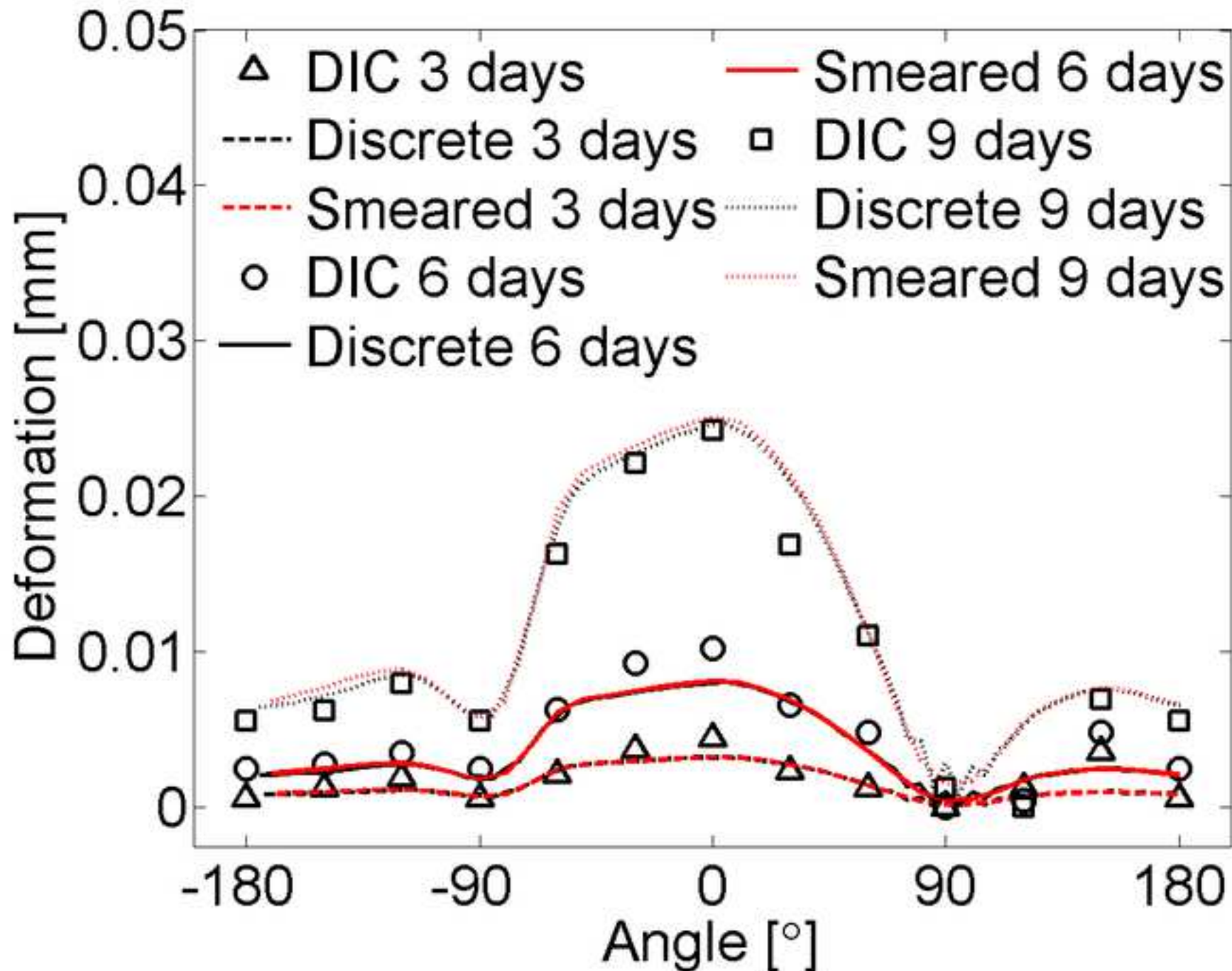


-  Original size of reinforcement
-  Non-corroded reinforcement
-  Expanded corrosion layer
-  Corroded reinforcement
-  Semi-infinite concrete body

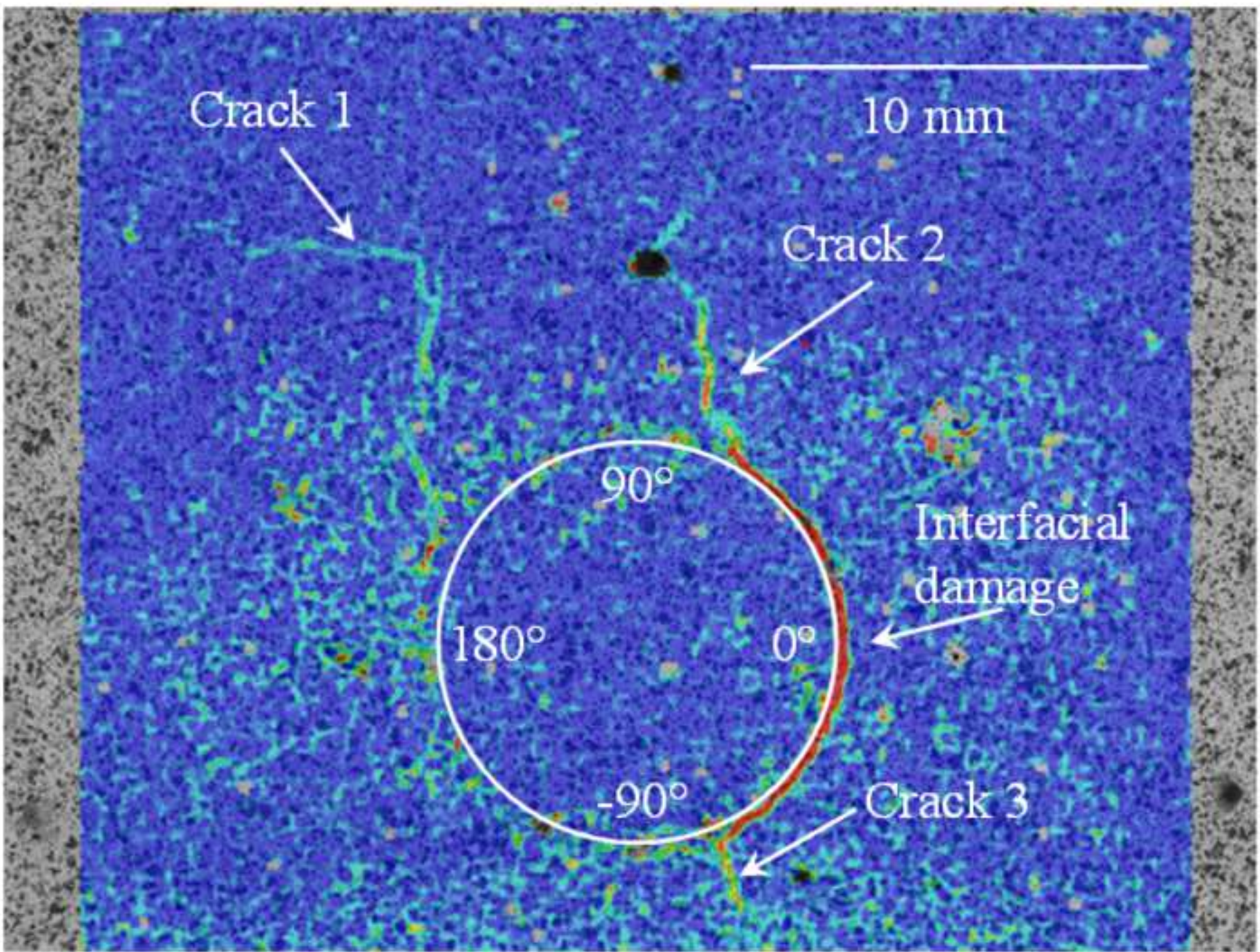
1
2
3
4
5
6
7
8
9
10
11
12
13
14
15
16
17
18
19
20
21
22
23
24
25
26
27
28
29
30
31
32
33
34
35
36
37
38
39
40
41
42
43
44
45
46
47
48
49

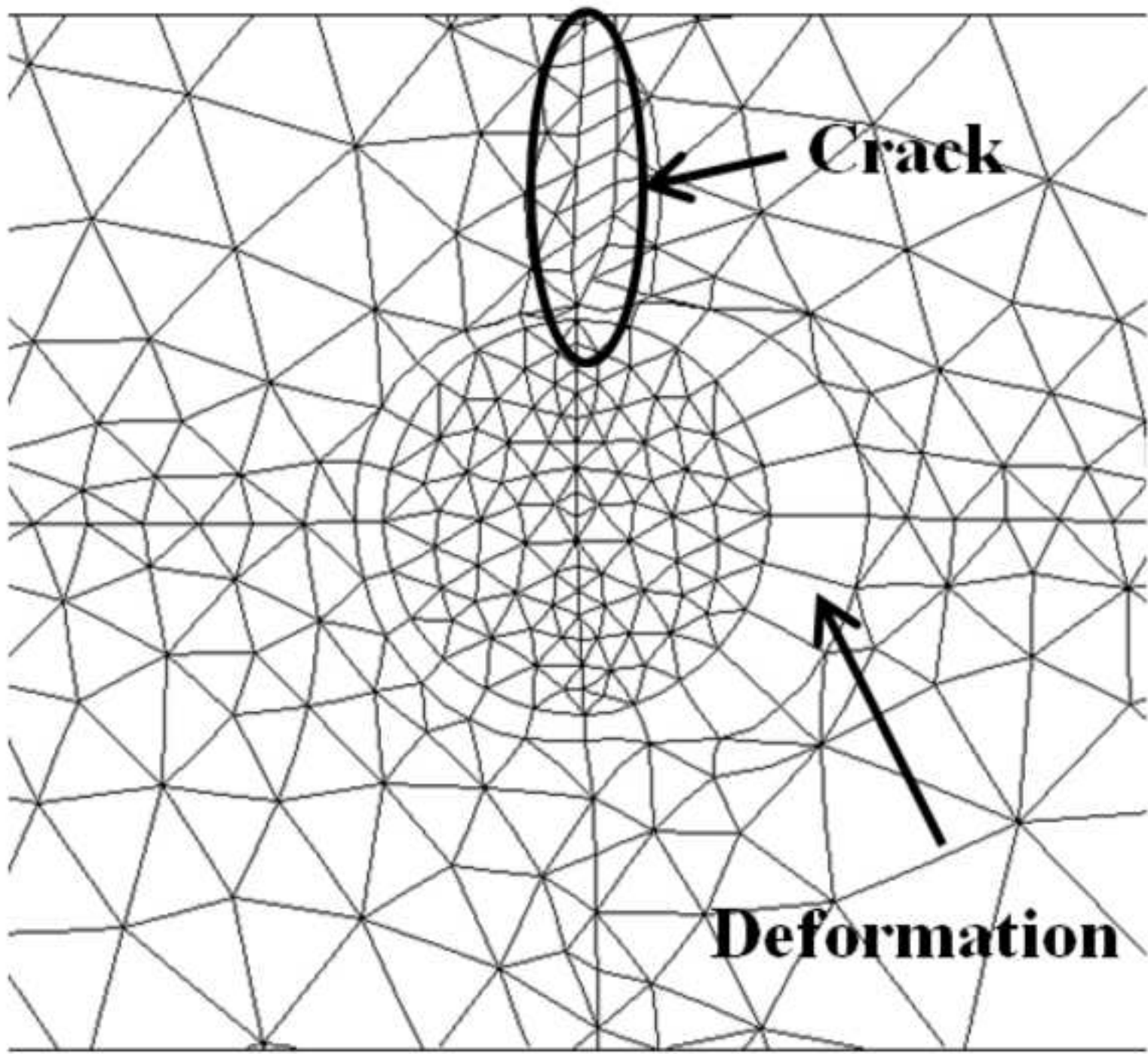
1
2
3
4
5
6
7
8
9
10
11
12
13
14
15
16
17
18
19
20
21
22
23
24
25
26
27
28
29
30
31
32
33
34
35
36
37
38
39
40
41
42
43
44
45
46
47
48
49



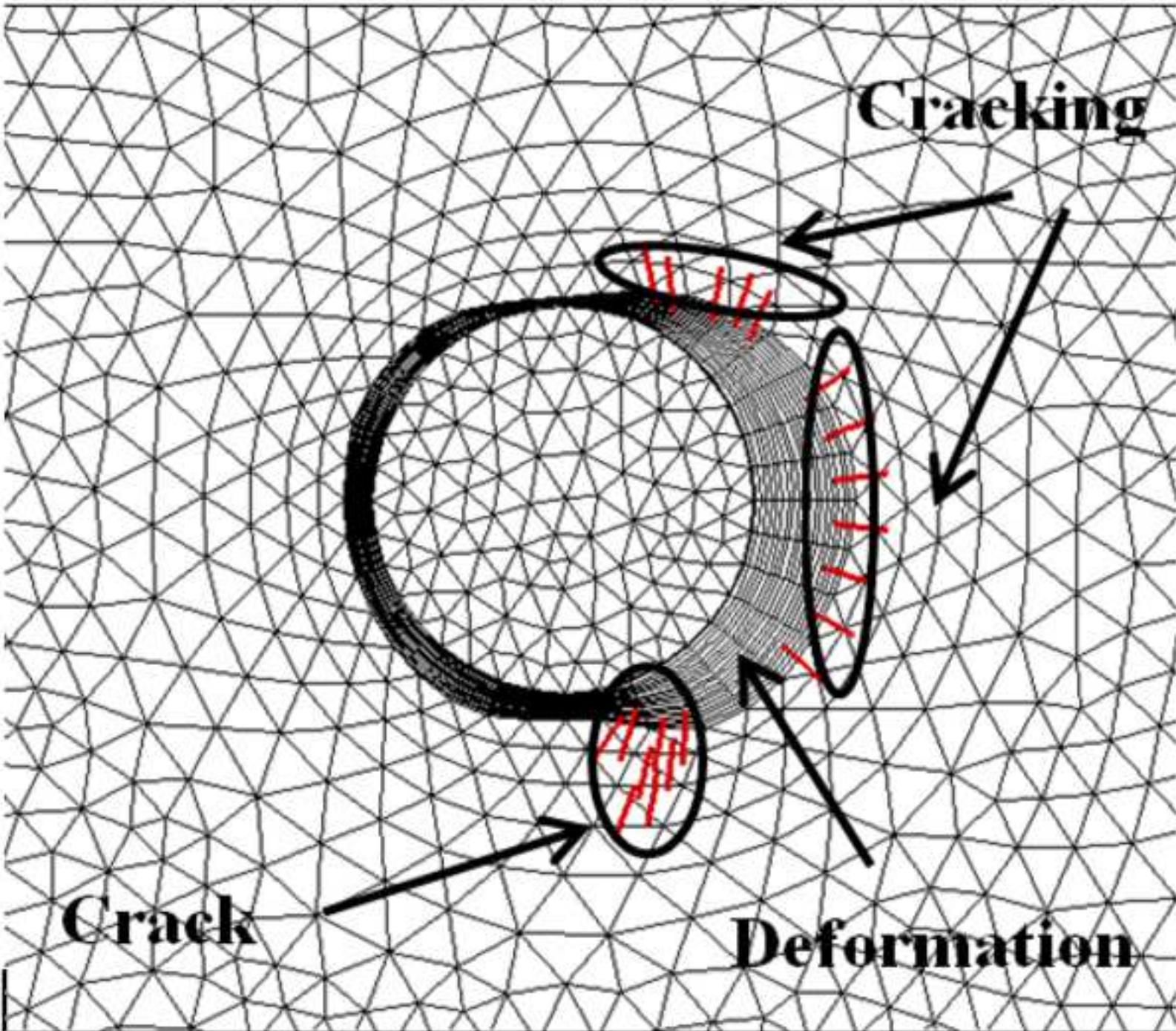
1
2
3
4
5
6
7
8
9
10
11
12
13
14
15
16
17
18
19
20
21
22
23
24
25
26
27
28
29
30
31
32
33
34
35
36
37
38
39
40
41
42
43
44
45
46
47
48
49

1
2
3
4
5
6
7
8
9
10
11
12
13
14
15
16
17
18
19
20
21
22
23
24
25
26
27
28
29
30
31
32
33
34
35
36
37
38
39
40
41
42
43
44
45
46
47
48
49

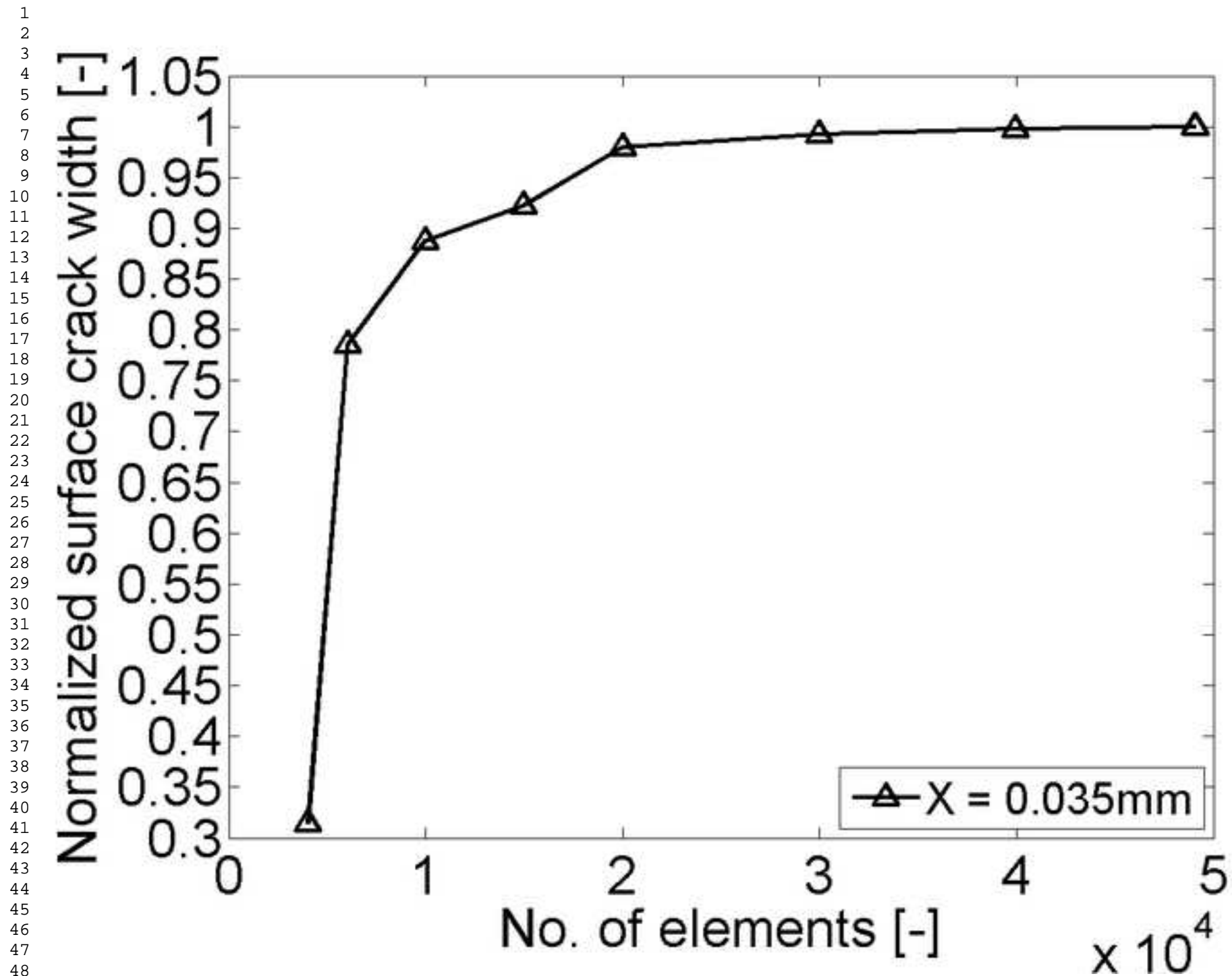




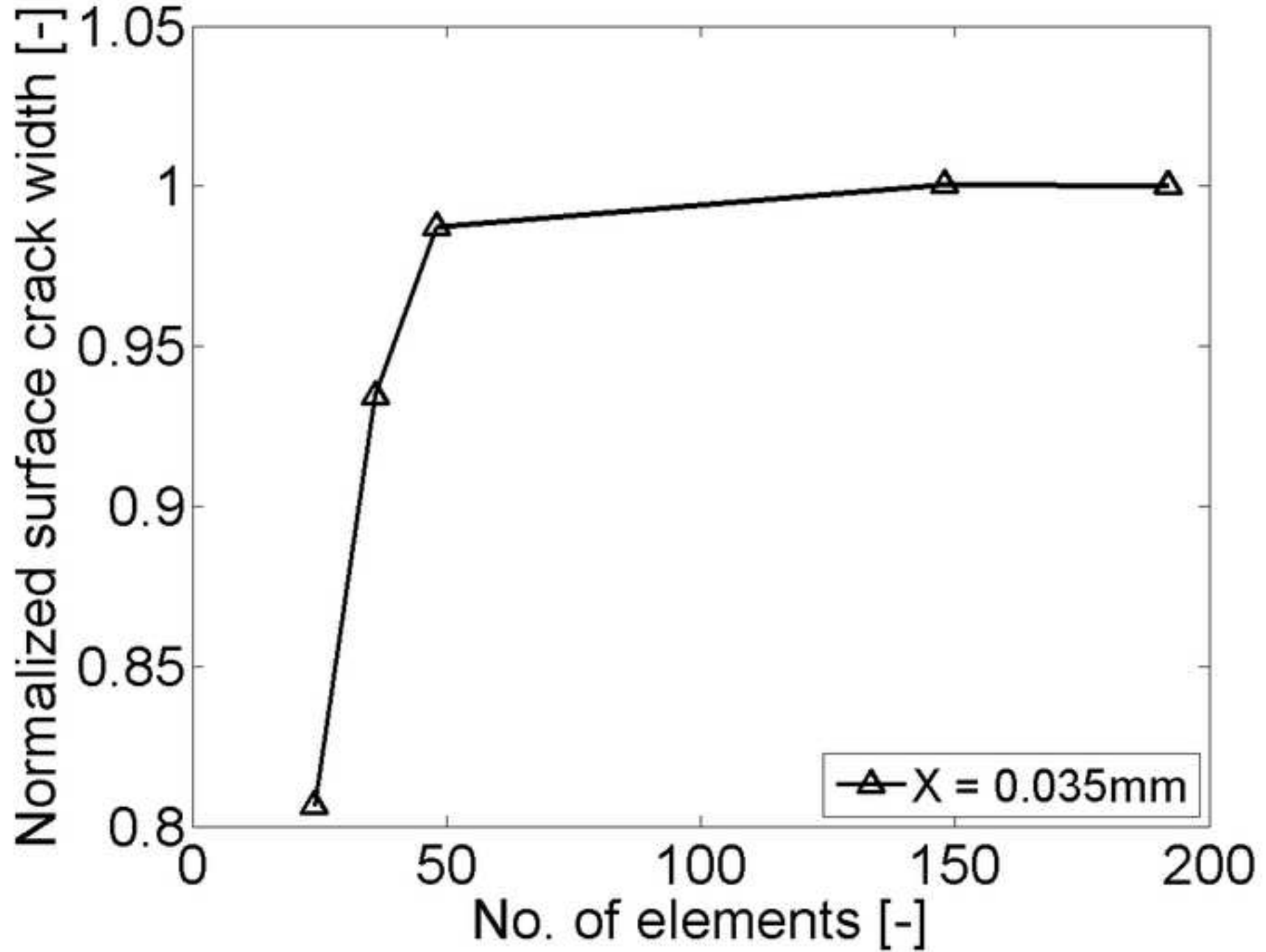
1
2
3
4
5
6
7
8
9
10
11
12
13
14
15
16
17
18
19
20
21
22
23
24
25
26
27
28
29
30
31
32
33
34
35
36
37
38
39
40
41
42
43
44
45
46
47
48
49

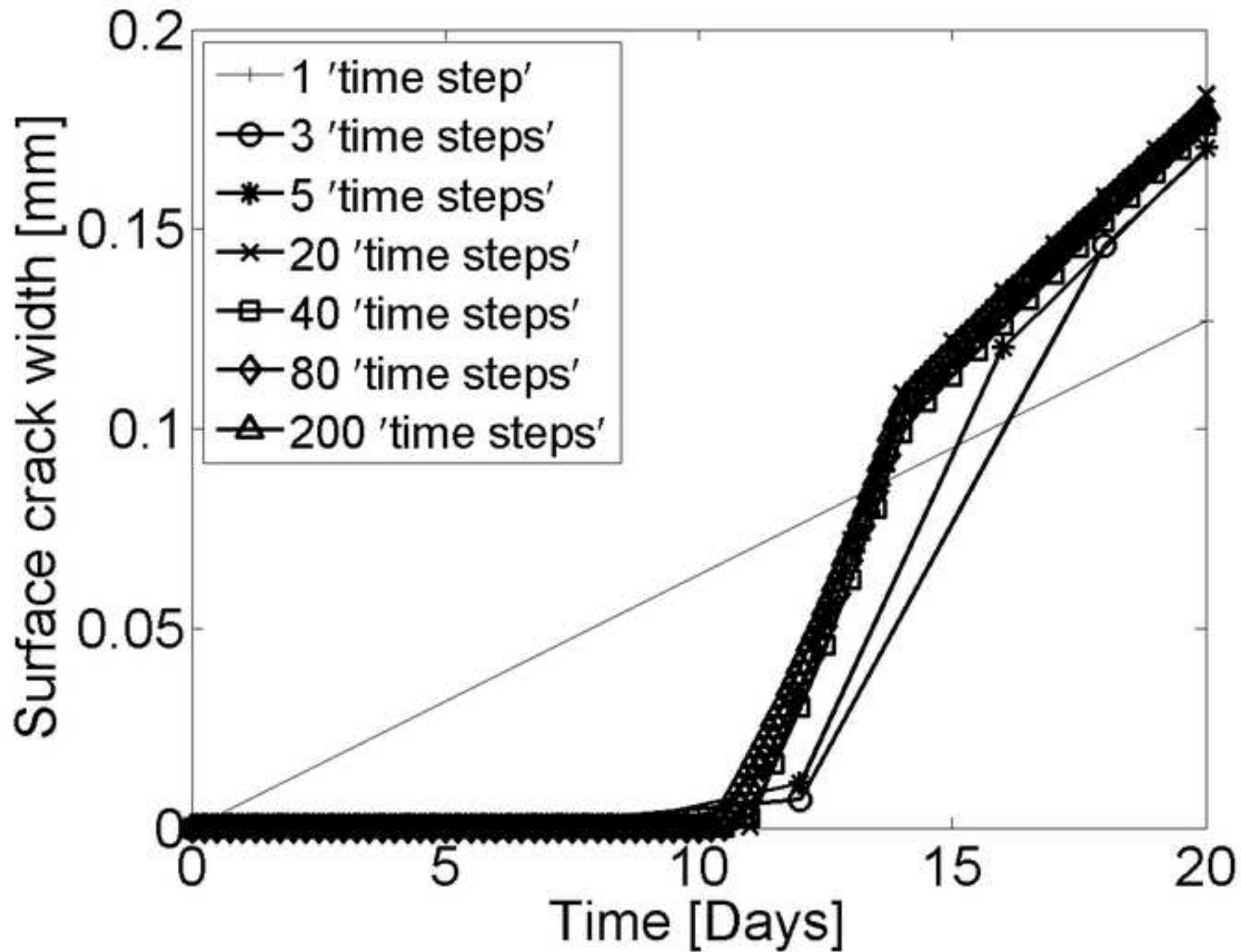


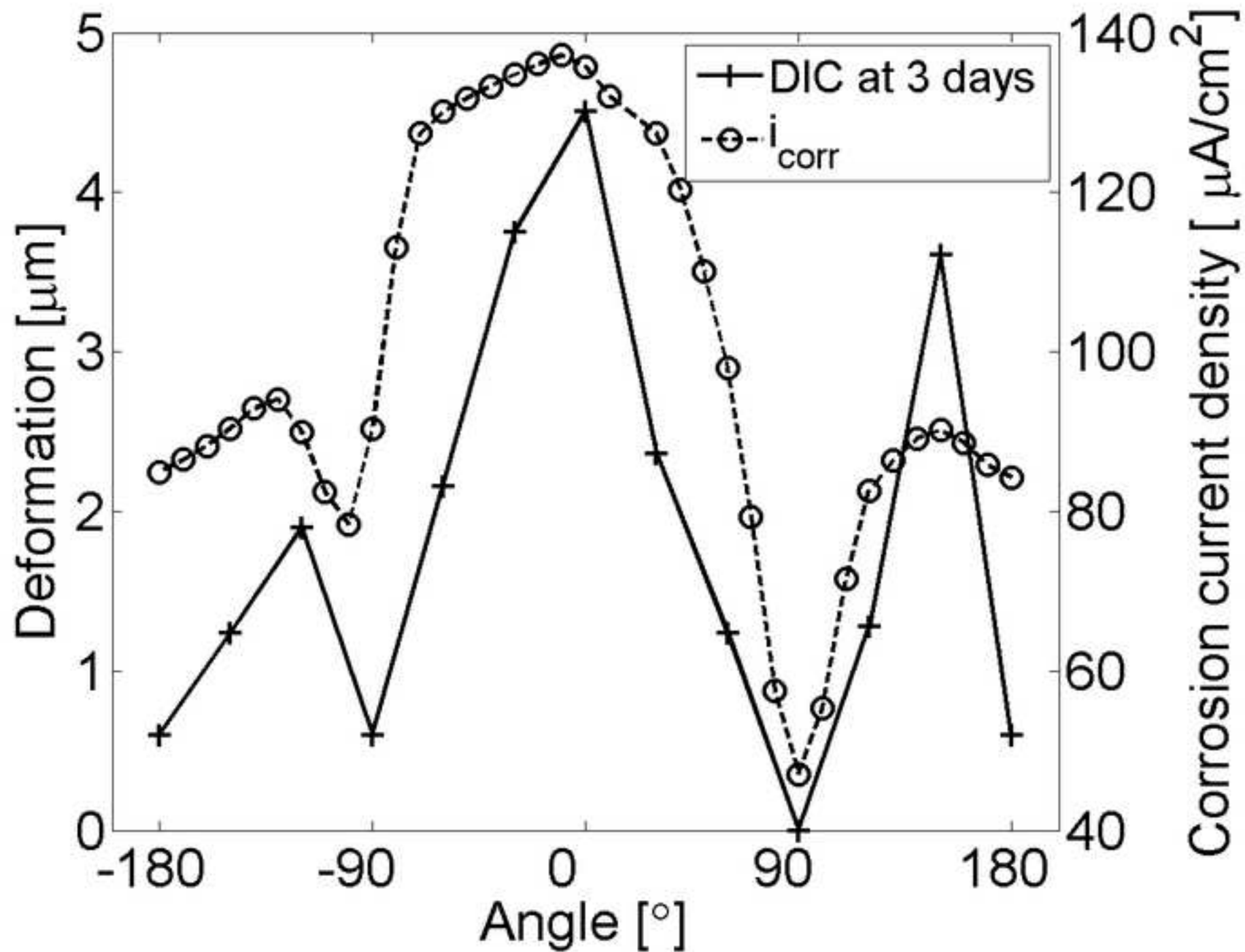
1
2
3
4
5
6
7
8
9
10
11
12
13
14
15
16
17
18
19
20
21
22
23
24
25
26
27
28
29
30
31
32
33
34
35
36
37
38
39
40
41
42
43
44
45
46
47
48
49

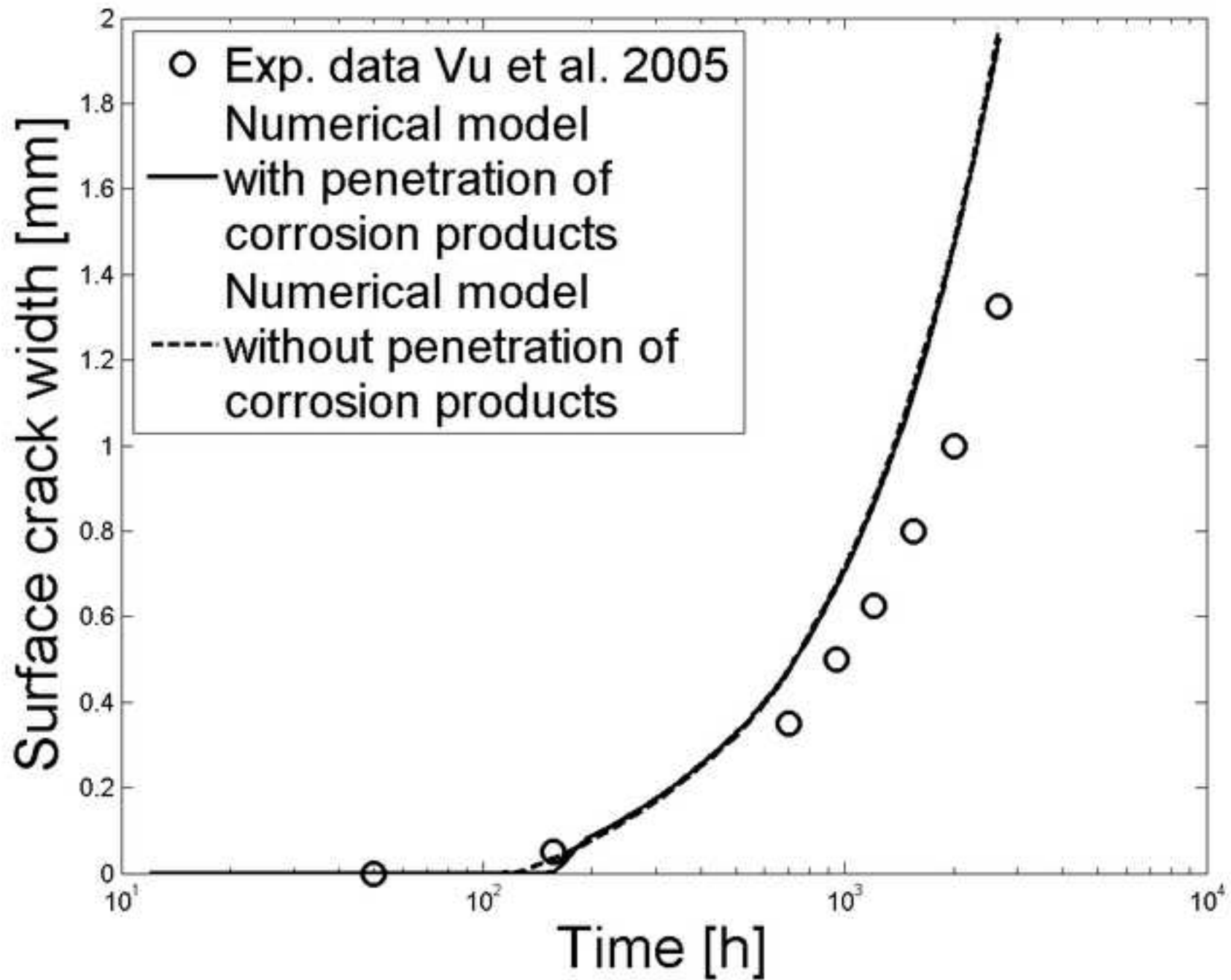


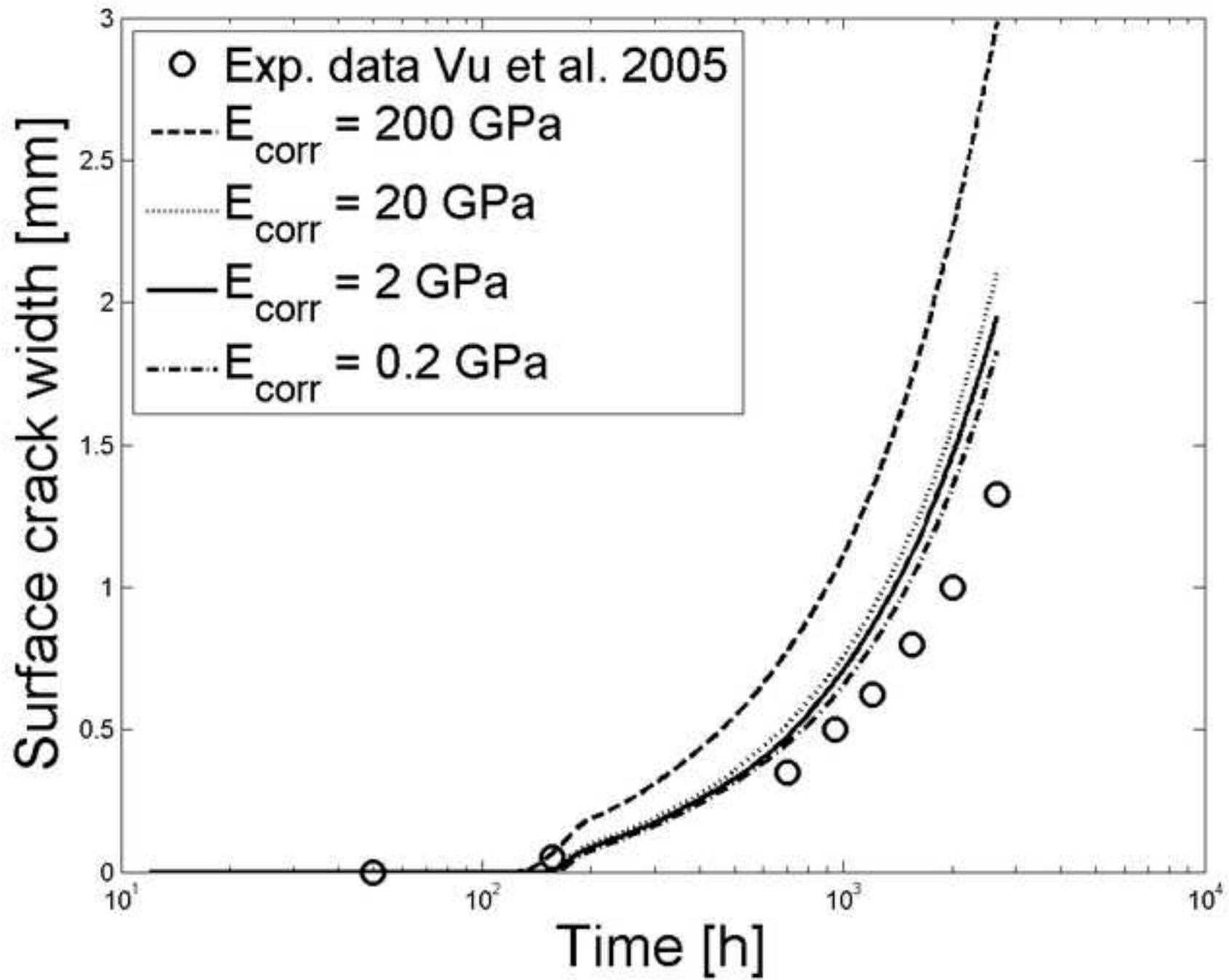
1
2
3
4
5
6
7
8
9
10
11
12
13
14
15
16
17
18
19
20
21
22
23
24
25
26
27
28
29
30
31
32
33
34
35
36
37
38
39
40
41
42
43
44
45
46
47
48
49

1
2
3
4
5
6
7
8
9
10
11
12
13
14
15
16
17
18
19
20
21
22
23
24
25
26
27
28
29
30
31
32
33
34
35
36
37
38
39
40
41
42
43
44
45
46
47
48
49

1
2
3
4
5
6
7
8
9
10
11
12
13
14
15
16
17
18
19
20
21
22
23
24
25
26
27
28
29
30
31
32
33
34
35
36
37
38
39
40
41
42
43
44
45
46
47
48
49

1
2
3
4
5
6
7
8
9
10
11
12
13
14
15
16
17
18
19
20
21
22
23
24
25
26
27
28
29
30
31
32
33
34
35
36
37
38
39
40
41
42
43
44
45
46
47
48
49

1
2
3
4
5
6
7
8
9
10
11
12
13
14
15
16
17
18
19
20
21
22
23
24
25
26
27
28
29
30
31
32
33
34
35
36
37
38
39
40
41
42
43
44
45
46
47
48
49

1
2
3
4
5
6
7
8
9
10
11
12
13
14
15
16
17
18
19
20
21
22
23
24
25
26
27
28
29
30
31
32
33
34
35
36
37
38
39
40
41
42
43
44
45
46
47
48
49